

Authors Version

Detrimental effects of sand ingress in jet engine ceramic coatings captured with Raman-based 3D rendering.

C. Barrett¹, Z. Stein², J. Hernandez², R. Naraparaju³, U. Schulz³, L. Tetard¹, S. Raghavan^{2*}

¹ Department of Physics, University of Central Florida, Orlando, Florida, 32816, USA.

² Department of Mechanical & Aerospace Engineering, University of Central Florida, Orlando, Florida, 32816, USA.

³ Institute of Materials Research, German Aerospace Centre (DLR), Cologne, 51170, Germany.

Detrimental effects of sand ingress in jet engine ceramic coatings captured with Raman-based 3D rendering.

C. Barrett¹, Z. Stein², J. Hernandez², R. Naraparaju³, U. Schulz³, L. Tetard¹, S. Raghavan^{2*}

¹ Department of Physics, University of Central Florida, Orlando, Florida, 32816, USA.

² Department of Mechanical & Aerospace Engineering, University of Central Florida, Orlando, Florida, 32816, USA.

³ Institute of Materials Research, German Aerospace Centre (DLR), Cologne, 51170, Germany.

Abstract

The infiltration of molten calcium, magnesium, and aluminosilicates (CMAS) into jet engine thermal barrier coatings (TBCs) causes an increased stiffness and a destructive phase destabilization eventually leading to thermomechanical failure. Using 3D confocal Raman spectroscopy, the extent of thermochemical degradation was identified by mapping the monoclinic phase volume fraction (mPVF) throughout a standard EB-PVD 7YSZ TBC coating. The mPVF is characterized as a function of depth and infiltration time with microscale resolution. Results show that phase destabilization was most intense along the column's perimeter whereas the core of the column retained most of its original phase. The greatest amount of phase destabilization occurs within the first hour of the interaction after which the average minimum mPVF is 32%. This value increases to 42% after a ten-fold increase in interaction time. This ability to quantitatively and non-destructively characterize degradation of CMAS infiltrated TBCs will accelerate development of degradation resistant coatings.

Keywords

CMAS, Thermal Barrier Coatings, 7YSZ, Non-Destructive, Confocal Raman Spectroscopy

1. Introduction

In order to increase engine efficiency, the operating temperatures of jet engines are pushed beyond the melting point of the underlying metallic alloys that make up their components [1]. Safe operation in this extreme environment is ensured by the use of thermal barrier coatings (TBCs) [2-4]. Common TBCs are composed of three layers on top of a metallic substrate: a ceramic top coat such as 7 wt.% yttria stabilized zirconia (7YSZ), a thermally grown oxide (TGO) layer, and a metallic bond coat [3]. A 7YSZ top coat is considered as a suitable model system. In this study, the top coat was deposited on an alumina substrate via electron beam physical vapor deposition (EB-PVD). This resulted in a characteristic segmented columnar structure, which provides high strain tolerance and thermal shock protection [5]. Also characteristic of the EB-PVD fabrication method is the presence of closed porosity throughout the coating, which lowers thermal conductivity of the TBC, further insulating the metallic engine components from high temperature degradation [6].

In flight, jet engine TBCs are exposed to several types of degradations [4, 7, 8], including airborne contaminants with a composition dominated by calcium, magnesium and aluminosilicates (CMAS) [9]. As TBCs make it possible to increase operating temperatures, the melting point of CMAS can be reached [6, 7], which can have detrimental effects on TBCs as molten CMAS infiltration can drastically alter their mechanical and chemical properties [10-16]. Infiltration is exacerbated by the capillary effect in TBCs obtained by EB-PVD [6, 17]. As the molten CMAS penetrates the ceramic topcoat, the YSZ oxide is dissolved in stoichiometric proportions and reprecipitates as yttria-depleted zirconia grains [7, 15, 16]. As a result, the metastable yttria-rich tetragonal phase (t' -ZrO₂) constitutive of EB-PVD YSZ TBCs transforms into the unstable yttria-lean tetragonal phase (t -ZrO₂). This, in turn, leads to the t -ZrO₂ phase reverting to the monoclinic phase (m -ZrO₂) upon cooling at ambient temperature [7, 11, 12, 16, 18]. The destabilization pathways of t' -ZrO₂ from high temperature exposure and from CMAS attack have been elucidated in previous reports [19, 20]. During rapid cooling, CMAS solidifies within the inter-columnar gaps and the porosity of the coating, effectively combining the open spaces and segmented micro-structure of the coating into a conglomerate, particularly at the surface of the TBC and at its interface with the metallic bond coat [16]. This conglomeration increases the modulus of the layer [15, 21], diminishes the strain tolerance and increases the thermal conductivity of the coating [15, 22, 23]. In addition, the t -ZrO₂ to m -ZrO₂ phase change

is accompanied by a volume expansion of approximately 3-5%, which further compromises the structural integrity of the coating, contributing to stress localization, crack propagation and spallation [15, 18, 21, 24-26]. CMAS infiltration depth depends on many factors such as the viscosity of the CMAS melt, the microstructure of the coating and the extent of thermal gradient [17]. It is known that the lifetime of a TBC under CMAS attack is dependent on the infiltration depth as well [27]. Up to the authors' knowledge, currently, there are no non-destructive analyses to identify the CMAS infiltration depth with high resolution in a TBC on real engine hardware. A novel technique must be developed in order to predict the TBC damage before the coatings undergo spallation and the blades exposed to high temperatures, which can eventually cause catastrophic incidents.

Raman spectroscopy uses inelastically scattered light to identify the chemical bonds present within a material and has the ability to distinguish between the different chemical phases of a material such as ZrO_2 [19, 28]. As a result, Raman spectroscopy is a powerful tool for the identification of the phase destabilization that occurs in CMAS-infiltrated coatings, which can help identify the extent of degradation as a result of CMAS infiltration [16, 19]. Furthermore, the confocality implemented on new Raman systems enables non-invasive probing below the sample surface to characterize the volume of TBCs without the need for cross sectioning.

Here, by creating 2D Raman hyperspectral maps at increasing depths within the coating, a 3D reconstruction was created tracking the degradation through the evolution of phase concentrations caused by the infiltration of CMAS into the ceramic coating. The phase degradation of EB-PVD 7YSZ due to the CMAS infiltration at 1250°C was studied in a novel manner as a function of time and depth using 3D confocal Raman spectroscopy [17, 29, 30]. We evaluated changes of monoclinic phase volume fraction (mPVF) in ZrO_2 at various depths and locations across 7YSZ by comparing the peak intensities of the m- ZrO_2 Raman bands to the sum of the intensities of the bands corresponding to the t- ZrO_2 and m- ZrO_2 phases following a method established by Clarke & Adar [31]. Using this method, a 3D map of the phase volume fractions in the EB-PVD 7YSZ system was reconstructed to show the effects of annealing time on the depth of the m- ZrO_2 phase formation with microscale resolution. The approach was validated by characterizing a cross section of the same sample with surface Raman measurements. Additionally, the distribution of the phase volume fractions with respect to the microstructure of the TBC was elucidated. SEM-EDS was used to further validate the results of the Raman confocal studies.

2. Material and methods

2.1 7YSZ Topcoat fabrication

7YSZ coatings (thickness of 400 μm) were produced on alumina substrates using a 150 kW EB-PVD system equipped with a single ingot containing 7YSZ at the German Aerospace Center (DLR) in Cologne, Germany. A thicker TBC was intentionally coated for fundamental study purposes and does not represent actual blade coatings. The alumina substrates were placed on a sample holder rotating directly above the ingot. The parameters for the TBC deposition included a substrate temperature of 1000 $^{\circ}\text{C}$ with a rotational speed of 12 rpm.

2.2 CMAS composition and fabrication

The CMAS composition (in mol.%: 24.6% CaO, 12.4% MgO, 11% Al₂O₃, 41.7% SiO₂, 8.7% FeO & 1.6% TiO₂) was derived from the compositions found in aero-engines operating in Middle Eastern countries and have been used in previous studies [6]. The CMAS powders were artificially synthesized through co-decomposition of Me-nitrates together with SiO₂ and TiO₂ powders, as described in more details in [6].

2.3 Sample preparation

A CMAS reference sample was prepared by annealing CMAS powder at 1250 $^{\circ}\text{C}$ for 10 h allowing it to melt onto a platinum foil. CMAS was applied as a paste in the amount of 10 mg/cm² on the 7YSZ coating and infiltration experiments were carried in a laboratory box furnace with heating/cooling rates of 10K/min. Two annealing times, 1 h and 10 h, were used. The list of

Table 1. Inventory of the samples considered in this study.

Sample	Composition	Annealing Temperature ($^{\circ}\text{C}$)	Annealing time (h)
C1	CMAS	1250	10
A0	7YSZ	0	0
A3	7YSZ	1250	10
B2	7YSZ+CMAS	1250	1
B3	7YSZ+CMAS	1250	10

samples considered in this study is provided in Table 1. Control samples composed of pure 7YSZ (A0, A3) were used as reference to rule out the effect of high temperature on 7YSZ and focus on the changes resulting from CMAS infiltrated in 7YSZ (samples B2 and B3). For validation, a cross section of the CMAS infiltrated TBC annealed for 10 h (B3) was prepared to collect Raman spectra directly from the volume corresponding to the depth probed with the non-destructive approach. Prior to cross sectioning, the samples were covered with an epoxy (Gatan G2), sectioned in half using a diamond saw and polished down to a 0.05 μm finish using standard metallographic techniques.

2.4 Sample characterization

Scanning electron microscopy images (SEM) of the cross sections of the infiltrated samples to assess the CMAS infiltration were obtained on a DSM Ultra 55 SEM (Carl Zeiss NTS, Wetzlar, Germany) equipped with energy dispersive spectroscopy (EDS) (Inca, Oxford Instruments Abingdon, UK) to determine the compositions of the crystalline phases.

Raman measurements were performed on an Alpha 300RA WITec Confocal Raman microscope with a He:Ne 532 nm laser source excitation and a 20X objective (Numerical Aperture 0.4, corresponding to Z-resolution of 6.65 μm and XY-resolution of 0.8 μm). For all data reported here, excitation laser power (11.6 mW) and collection parameters remained constant, including an integration time of 20 s. After filtering the Rayleigh scattering with a notch filter, the inelastically scattered light was split with an 1800 gr/mm grating. Step size of 1 μm was used for the line scans and 2D maps. 2D maps consisted of an array of 20 x 20 spectra (this corresponded to 400 spectra collected in a total acquisition time of 8,000 s per 2D map). Detection covered the spectral range of 100 – 800 cm^{-1} . To assess the CMAS degradation and the corresponding phase changes in 7YSZ as a function of depth, Raman point spectra and 2D spectral maps at increasing depths were collected by focusing the light at different positions beneath the surface. The step size between the different planes of analysis was to 6.65 μm , corresponding to the axial limit of resolution of the 20x objective.

3. Calculations

3.1 Determination of mPVF

We evaluated changes in the mPVF of ZrO₂ at various depths and locations across the model TBC by comparing the peak intensities of the m-ZrO₂ Raman bands to the sum of the intensities of the bands corresponding to the tetragonal (I_t^{148} , I_t^{263}) and monoclinic (I_m^{182} , I_m^{191}) phases following a model established by Clarke and Adar [31]:

$$\text{mPVF} = \frac{I_m^{182} + I_m^{191}}{0.97 * (I_t^{148} + I_t^{263}) + (I_m^{182} + I_m^{191})} \quad (1)$$

In this study, we considered the factor 0.97 used by Clarke and Adar [31] to be a satisfactory approximation given that our laser illumination is similar to the 514 nm source used to establish the reported factor.

The tetragonal phase volume fraction (tPVF) following a model established by Perry et al [32] using the intensities of the bands corresponding to the tetragonal (I_t^{263}) and monoclinic (I_m^{182}) phases:

$$\text{tPVF} = \frac{I_t^{263}}{(I_t^{263} + I_m^{182})} \quad (2)$$

3.2 Analysis of Raman spectra

In order to calculate the mPVF, the bands of the corresponding Raman shifts were fitted using a pseudo-Voigt function. The pseudo-Voigt function approximates the Voigt function that is a convolution of Gaussian and Lorentzian profiles [33, 34]. It assumes equal line widths of both Gaussian (Eq. 2) and Lorentzian (Eq. 3) profiles. The pseudo-Voigt profile has been found to be a good approximation to the Voigt function based on analysis of several spectra [35].

The nonlinear least squares solver in MATLAB was used for curve fitting in order to determine the intensity of the selected bands. The intensities of the Raman bands corresponding to the monoclinic phase at 182 cm⁻¹ and 191 cm⁻¹ and to the tetragonal phase at 148 cm⁻¹ and 263 cm⁻¹ were calculated using the pseudo-Voigt fit. The 2D and 3D representations of the mPVF variations in the sample were constructed with MATLAB using a cubic spline interpolation smoothing to reduce pixilation and produce a gradient in the final rendering. The 3D maps were

compiled by importing the sequence of 2D maps into the volume viewer plugin of ImageJ, using a z-aspect ratio parameter of 100 and a sampling parameter of 20 with a trilinear interpolation.

Box and whisker plots were generated to display the data as the median mPVF measured as a function of depth. The central line corresponds to the median, while the bottom and top edges of the box indicate the 25th and 75th percentiles, respectively. The whiskers indicate the maximum and the minimum mPVF values and are not considered as outliers.

4. Results

A representation of the morphological of the CMAS infiltrated 7YSZ TBC after 10 h of CMAS infiltration at 1250°C is presented in Fig. 1. Fig. 1(a) shows the top 50 μm of the coating at the CMAS-7YSZ interface whereas Fig. 1(b-e) represent the microstructure at distances of 100, 200, 300 and 400 μm from the surface, respectively. In Fig. 1(a-d), large gaps of several micrometers were present, which were attributed to CMAS-associated sintering of the columns. Gaps observed in Fig. 1(e) were smaller. However, a large amount of deposits, which are likely a reservoir of CMAS, can be observed in the lower part of the coating, at the interface with the substrate, in Fig. 1(e). At the top of the TBC, the red lines in Fig. 1(a) were drawn to differentiate the reacted (outside of the line) and un-reacted (inside the line) regions of 7YSZ of the columns. CMAS was present in heterogeneous pockets at the periphery of the columns. Structural changes due to CMAS attack on the coating could be observed as well as more rounded edges (red arrows) of the columns that were

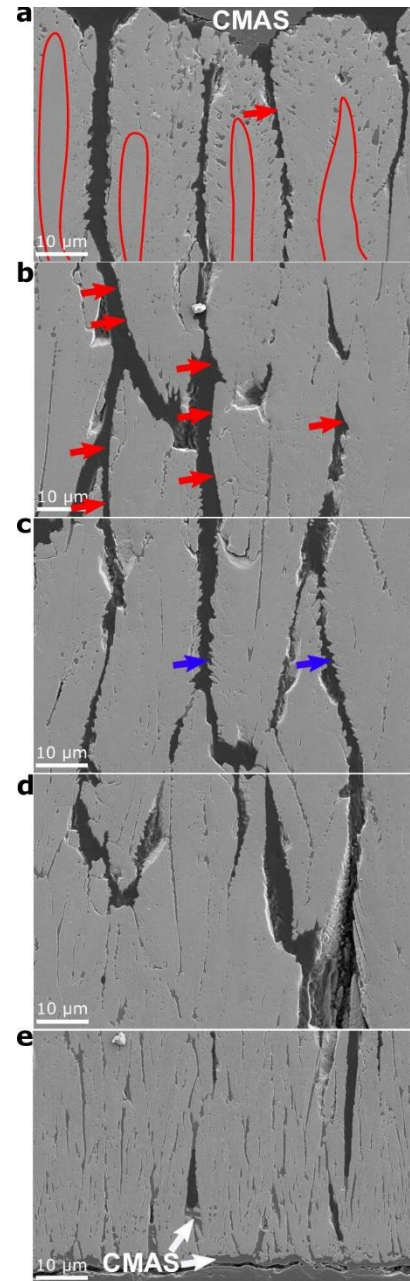


Fig. 1. Microstructural changes to the TBC columns as a result of dissolution in steps of 100 μm after 10 h of CMAS infiltration at 1250 $^{\circ}\text{C}$. SEM images obtained at selected depth below surface: (a) 0 μm (b) 100 μm (c) 200 μm (d) 300 μm (e) 400 μm . Red arrows indicate regions with most severe loss in feathery features, while regions least affected are shown by blue arrows.

originally more “feathery” (blue arrows) in appearance. “Feathery” edges that are more representative of the pristine TBC (Fig. S1(a)) could be observed in some columns of the images collected at 200 μm (Fig. 1(c)), but not at the surface nor at depths of 300 and 400 μm (Fig. 1(d,e)). These observations are in agreement with previous work by Naraparaju et al [6].

4.1 Raman spectra of pure CMAS and 7YSZ

Next, the effect of the aforementioned infiltration on the phases of ZrO_2 was investigated by Raman confocal microscopy. Molten CMAS was first characterized by Raman spectroscopy (Fig. 2(a)). Several bands in the 100 - 800 cm^{-1} range are consistent with the 3D network of SiO_4 and AlO_4 tetrahedra in CMAS [36], with various ions including calcium, magnesium, and, to a lesser extent, titanium and iron modifying its network. Raman modes above 500 cm^{-1} were previously attributed to vibrational modes associated with bonds between the silicon, aluminum and oxygen ions [36, 37]. Bands below 500 cm^{-1} likely correspond to a perturbation of the vibration of the SiO_4 tetrahedra by the different ions found in CMAS. For instance, the band located around 192 cm^{-1} has been ascribed to SiO_4 tetrahedra being modified by magnesium ions [38-40] while the bands around 343 cm^{-1} and 398 cm^{-1} likely correspond to SiO_4 tetrahedra affected by the presence of calcium ions [41-43], and iron ions [39, 41], respectively.

Characteristic Raman signatures of the tetragonal phase of 7YSZ before annealing (sample A0) and after annealing (sample A3) are shown in Fig. 2(b). Raman signatures of the non-reacted samples (samples A0 and A3) exhibit six characteristic bands at 148 cm^{-1} , 263 cm^{-1} , 322 cm^{-1} , 466 cm^{-1} , 610 cm^{-1} , and 642 cm^{-1} , consistent with previous reports on the tetragonal phase of zirconia found [19, 44-46]. An effect of high temperature on the TBC without CMAS attack was observed after annealing without CMAS (sample A3). A marked increase in the 263 cm^{-1} peak intensity was observed in addition to a shift (Fig. 2(b)). The increase in intensity may be attributed to a change in the zirconia lattice due to heating [47]. Furthermore, it is noticed that the peak located at 263 cm^{-1} narrowed, which is indicative of an increase in the local order of the crystalline lattice [28].

4.2 Probing the depth of the CMAS infiltrated 7YSZ with Raman confocal spectroscopy

CMAS degradation and the corresponding phase changes in 7YSZ were evaluated with Raman confocal spectroscopy. Spectra presented in Fig. 2(c) were collected at increasing depths. Monoclinic bands (182 cm^{-1} , 192 cm^{-1}) that were not present in samples A0 and A3 (Fig. 2(b))

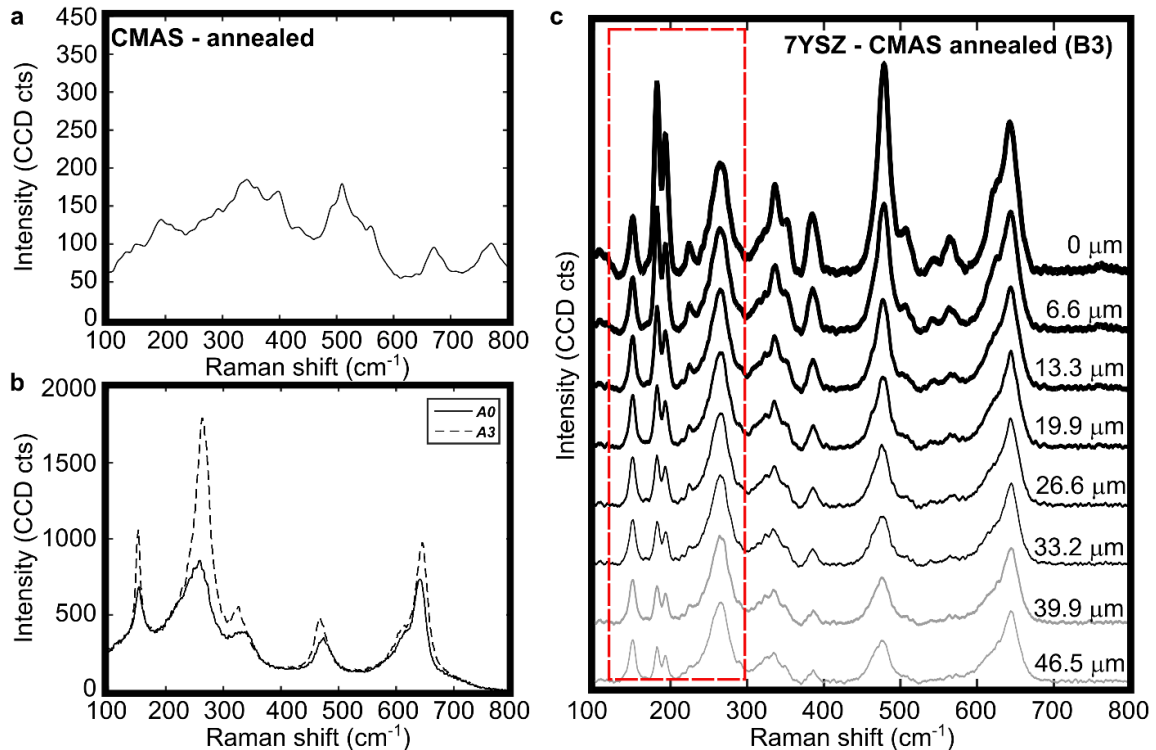


Fig. 2. Raman spectra of the materials involved in the CMAS-7YSZ interaction. (a) Raman spectrum of CMAS after annealing at 1250°C for 10 h. **(b)** Raman spectrum of 7YSZ alone before and after annealing. **(c)** Evolution of Raman spectrum of 7YSZ as a function of depth within the coating – a depth of $0\mu\text{m}$ corresponds to the surface of the sample

could be observed in the infiltrated TBC. Intensities of all the bands decreased with increasing depth, although the rate at which the monoclinic peak intensities decreased was much greater than that of the tetragonal bands. The part of the 7YSZ coating analyzed by confocal Raman spectroscopy shown in Fig. 2(c) corresponds to the top 50 μm of 7YSZ coatings shown in Fig. 1(a).

4.3 Validation of confocal Raman spectroscopy depth measurements

The framework of non-destructive characterization of phase destabilization due to CMAS infiltration was validated by comparing the Raman data collected on the non-sectioned B3 sample (volume probing in Fig. 2(c)) and on the surface of the same sample that was cross-sectioned (surface probing) as depicted in Fig. 3(a). Fig. S2 provides the details of the locations probed for the non-sectioned and cross-sectioned samples. Fig. 3(a) depicts the measurement directions for the depth profiles and for the line scans performed on the cross-sectioned sample. Line scans, which correspond to a succession of spectra collected every 1 μm along a selected line, at the surface of the cross sectioned sample, allowed for data to be obtained at the center of the TBC column and at the perimeter of the TBC column. In addition, the representation of the locations at which the spectra were collected are depicted in blue for the edge of the column and red for the center of the column in Fig. 3(a). The data was used to elucidate the effect of microstructure on phase transformation due to CMAS ingress. Raman spectra were collected and fitted at each point and mPVF was calculated following eq. 1.

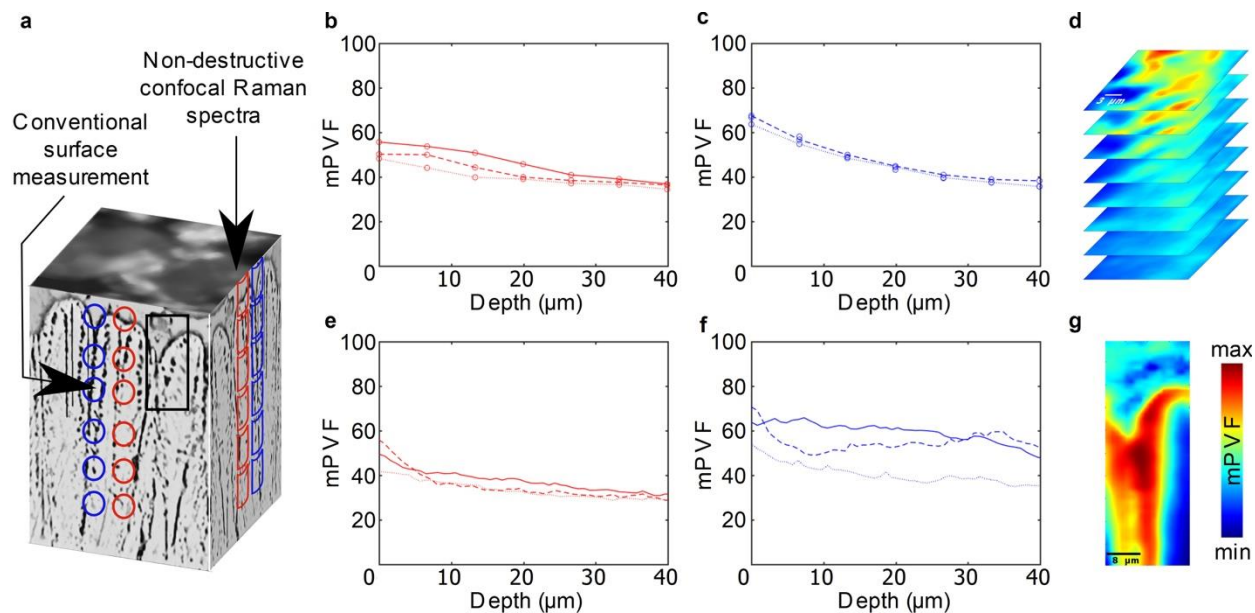


Fig. 3. Comparison of 3D confocal Raman spectroscopy and cross-section Raman spectroscopy. (a) Representation (not to scale) of a 3D volume of CMAS infiltrated EB-PVD 7YSZ used for validation of the 3D confocal Raman spectroscopy approach for non-destructive analysis. **The rectangles represent the data points acquired at the edge (blue) and center (red) of the column as a depth measurement with 3D confocal Raman spectroscopy. The circles represent the data points acquired at the edge (blue) and center (red) of the column as a surface measurement.** (b-d) mPVF measured on the unsectioned B3 sample using non-destructive depth probing at (b) the center, and (c) the perimeter of column. The three curves in each graph represent triplicates. (d) Successive 2D maps of mPVF obtained selected Z planes, i.e., depths. Scale bar indicates 3 μ m. (e-g) mPVF measured on the cross-sectioned B3 sample. Raman spectra collected along (e) the center, and (f) the outer layer of the column. The three curves in each graph represent triplicates. (g) Map of mPVF capturing one edge and center of a column in the section **as represented by the black box in (a)**. Scale bar indicates 8 μ m.

The mPVF determined from the cross sectioned sample at the center and perimeter of the TBC columns are shown in Fig. 3(e) and (f), respectively. A decrease in mPVF with increasing depth was observed in both locations, but the values for the mPVF along the outer layer of the columns were higher than in the center column throughout the depth. The data collected from the non-destructive depth profiles exhibited a similar behavior (Fig. 3(b,c)). To further demonstrate the lateral variation of the mPVF, the mPVF was mapped at the CMAS-7YSZ interface as shown in Fig. 3(g). The 2D maps (Fig. 3(d)) used for the 3D reconstruction (Fig. 4) also indicated similar changes in ZrO₂, more predominant in the outer layer of the columns. The lateral variation corresponds with the true interface seen in the SEM image in Fig 1(a) delineating the reacted and non-reacted regions.

4.4 Quantification of the effect of annealing time on phase transformation

Starting from the surface of the TBC, Raman spectra were collected in the form of 2D Raman spectral maps at focal planes at successive depth increases of $6.65 \mu\text{m}$ (see Methods). In order to quantify the effect of annealing time on the phase transformation due to CMAS infiltration, measurements were performed on two samples with different annealing times at $1250 \text{ }^\circ\text{C}$: B2 (1 h) and B3 (10 h). The Raman spectra collected were processed to calculate the tPVF and the mPVF in the volume probed (see Methods).

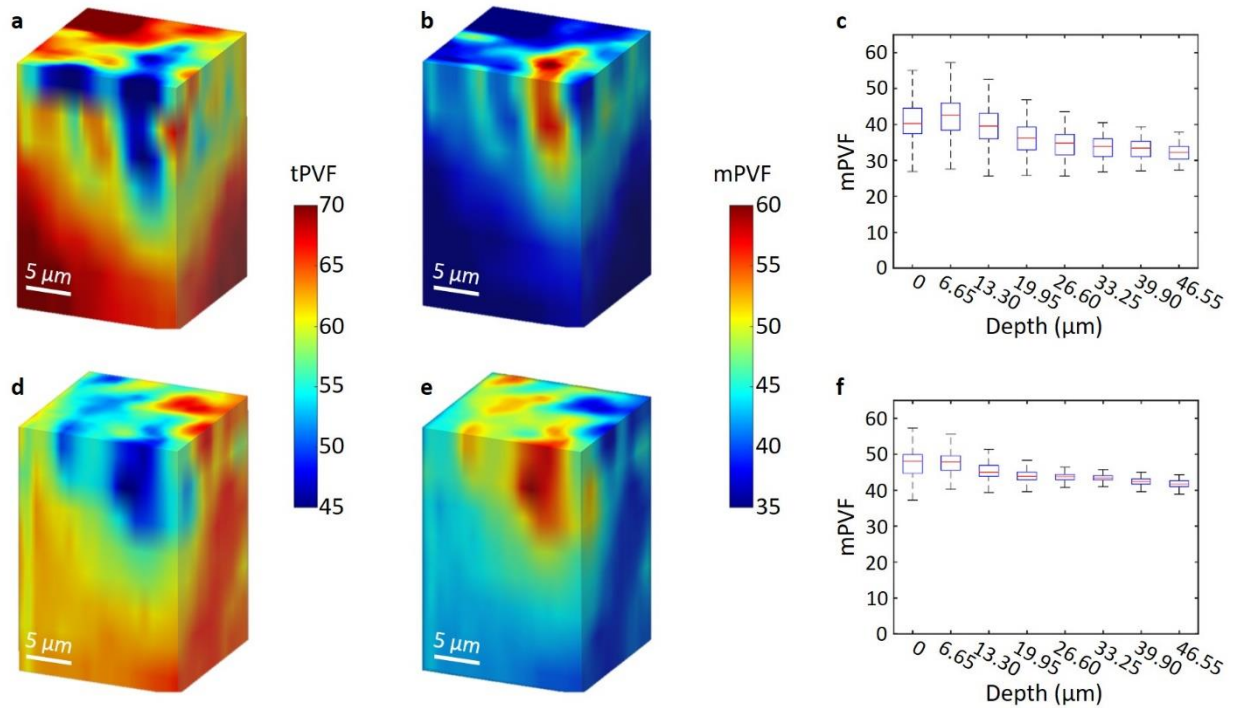


Fig. 4. Effect of increasing annealing time on CMAS infiltration in a volume of 7YSZ coating. 3D reconstruction of (a) tetragonal and (b) monoclinic phase volume fractions of B2 sample (1 h annealed) (c) Variation of mPVF along the depth in B2 (d) tetragonal and (e) monoclinic phase volume fractions of B3 sample (10 h annealed). and (f) Variation of mPVF along the depth B3 sample.

Table 2. Mean mPVF values per depth and their corresponding standard deviations extracted from the data presented in Fig. 4.

Depth (μm)	Sample B2		Sample B3	
	Mean mPVF (%)	Standard Deviation (%)	Mean mPVF (%)	Standard Deviation (%)
0	40.1	8.4	47.1	4.2
6.65	41.3	10.2	47.9	3.5
13.30	39.0	6.3	45.4	3.1
19.95	35.8	6.4	43.9	2.1
26.60	34.5	4.7	43.6	1.6
33.25	33.6	3.6	43.3	1.3
39.90	33.2	2.9	42.3	1.2
46.55	32.3	2.4	41.8	1.2

The 3D reconstructions of the tPVF of a $20 \times 20 \times 50 \mu\text{m}^3$ volume of the upper part of the top coat of samples B2 and B3 are presented in Fig. 4(a,d), respectively. Fig. 4(b,e) display the mPVF of the same volume in each sample. Overall, it can be observed that the values of the mPVF in sample B3 were roughly 10% higher than the values in sample B2. The variations of the mPVF values across the scanning plane as a function of depth are depicted in the box and whisker plots of Fig. 4(c) and (f) for samples B2 and B3 respectively, representative of the 400 spectra collected at each focal plane (see Methods). As shown in Table 2, for sample B3, the mean mPVF is found to be 41.8 % at a depth of 46.55 μm , while the mean mPVF in B2 at the same depth is 32.3 % at the same depth. It can also be seen that with an increased heating time the values of the mPVF become more constant as is shown by the decrease in the standard deviation from the mean values of the mPVF (Table 2). Throughout the depth of the coating the standard deviation for the mPVF values for sample B2 is double the standard deviation values for the mPVF values in sample B3, suggesting more heterogeneities in the system.

4.5 SEM investigation of the 7YSZ infiltrated with CMAS at 1250°C for 10h

To confirm our findings, a detailed microstructural analysis of sample B3 was performed under SEM. It provides an independent way to correlate the non-destructive confocal Raman results with a conventional destructive analytical technique to evaluate and confirm the CMAS infiltration/degradation. Fig. 5 shows an SEM image (Fig. 5(a)) and EDS mapping (Fig. 5(b-f)) of sample B3 at the 7YSZ-alumina interface. EDS mapping of Zr, Ca, Mg, Al and Si shown in Fig. 5(b-f) indicate that the CMAS infiltration reaches the 7YSZ-alumina interface through the inter-columnar gaps and fills open porosity (Fig. S1) throughout the coating after 10 h. Accumulation of CMAS at the 7YSZ-alumina interface is clearly visible from the elemental maps in Fig. 5. Figures S3 and S4 provide the details of the specific locations and corresponding elemental compositions of the CMAS from the EDS, respectively, confirming the accumulation of Si, Ca and O at the 7YSZ-alumina interface.

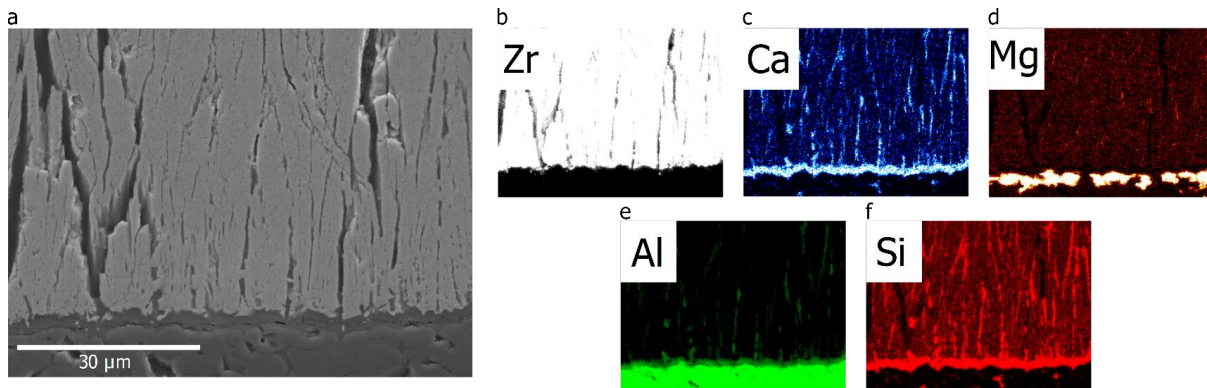


Fig. 5. 7YSZ coating infiltrated by CMAS. (a) SEM cross section image of CMAS-infiltrated 7YSZ EB-PVD coating close to the substrate. Elemental maps of (b) zirconium (Zr), (c) calcium (Ca), (d) magnesium (Mg), (e) aluminum (Al), and (f) silicon (Si).

5. Discussion

These results present the first known use of Raman confocal measurements to quantify, localize and delineate the reacted and unreacted 3D volumes with high spatial resolution, non-destructively. Fig. 1 shows the microstructural changes due to the CMAS infiltration for 10 h into the TBC throughout the coating. The large presence of the CMAS filled gaps, and the deteriorated edges of the outer regions of the columns confirm the degradation of the coating and

suggest that accumulation of the CMAS at this interface is accompanied by a thermochemical reaction. Presence of this accumulation is confirmed by the EDS mapping of the components of CMAS in Fig. 5(b-f).

The CMAS filled open spaces and can also be found throughout the coating as shown in Fig. 1(a-e). However, the degradation is not uniform. At the center of the coating (Fig. 1 (b-d)) fewer microstructural changes have been observed. This is due to the fact that reactions in the bulk of the coating are minimized by the limited availability of the melt in relation to the TBC material. In the studied case, molten CMAS is mainly at the CMAS-7YSZ and 7YSZ-alumina interface as shown in Figs. 1 and 5. In line with previous literature [16], the outer regions of the columns will be quickly infiltrated and slowly undergo phase transformation during cooling. This is clearly shown in Fig. 3(g) where most of the tetragonal phase remains at the center of the column, while the edges exhibit a very high mPVF content. A detailed study on the erosion properties of CMAS infiltrated EB-PVD 7YSZ with two different microstructures revealed that more ‘feathery’ microstructures are more susceptible to erosion **due to heavier reaction** [48]. In turn, it is expected that the mechanical properties of these columns will change severely due to the transition to m-ZrO₂ phase [15, 21]. At the 7YSZ-alumina interface (Fig. 1(e) and Fig. 5), the large accumulation of CMAS could lead to severe reactions of the columnar roots and result in the formation of more globular monoclinic grains (Fig. S1(b)) because of the TBC material being able to react with the higher availability of the CMAS melt present [16].

The bands observed in the Raman spectrum of CMAS (Fig. 2(a)) do not appear in the Raman spectrum of CMAS infiltrated 7YSZ (Fig. 2(c)) which only exhibits bands corresponding to the different phases of 7YSZ. To test the influence of heating the 7YSZ TBC without CMAS on its Raman signature, the spectra of the as coated sample (A0) and the sample heated for 10 h (A3) were compared. As noted earlier there is a minor effect of heating in that it seems to add order to its crystal lattice. However, it can be seen that simply heating pure 7YSZ under the conditions used for B3 did not induce any monoclinic phase. It was then concluded that the appearance of the monoclinic bands was due solely due to the 7YSZ-CMAS interaction. Further after the interaction occurs a decrease in the monoclinic band intensity as a function of depth was resolved with Raman spectroscopy as shown in Fig. 2(c). This led to the conclusion that it is possible to track the degradation of the coating as a function of depth with confocal Raman spectroscopy with negligible influence of CMAS on the Raman spectrum.

To ensure that the depth measurements were reliable, a comparison of Raman depth profiles performed on the intact sample (B3) and line scans performed on a cross-sectioned copy of sample B3 is presented. In this study, due to the size of the volume probed with Raman confocal microscopy, a difference in the mPVF was found depending on where the data was collected relative to the center of the columns. Given the difference in orientation of the volume probed when collecting depth profiles (Fig. 3(b,c)) and the line scans (Fig. (3(e,f))), we expect differences in shape of the Raman bands analyzed. Furthermore, the effect of the microsampling to distinguish gradients in properties in a complex matrix was previously discussed by Lipkin et al [49]. Keeping these variations in mind, the mPVF calculated from the standard Raman measurements performed on the cross-sectioned TBC and the non-invasive depth profile were compared, at the column's outer layer and at its center. At the center, mPVF values obtained using the depth profiles (Fig. 3(b)) and the line scans (Fig. (3(e))) show similar evolution of the properties in the volume of the TBC. At the perimeter of the columns, both collection methods show a higher value than at the center. This is due to the perimeter of the columns being in direct contact with the molten CMAS, which is in agreement with previous reports [16, 48, 50]. This constitutes the first reported map (Fig. 3(g)) of this phenomenon with such spatial resolution. Such maps make it possible to confirm that the CMAS attack is not as strong in the center columns of the coating. Although the non-destructive Raman measurement is in good agreement with the more conventional approach of sectioning the sample and probing its surface, we observe small differences in the evolution of mPVF content between the two data sets. Beside the aforementioned effect of the probe [49], this could also be attributed to the fact that columns are not perfectly vertical, making it difficult to predict where to probe when analyzing the material non-destructively. It is possible that during depth profiling, regions slightly out of the column's edges were probed. Even so, the two data collection methods appear to be in good agreement with each other.

With this validation of the method, the reconstruction of the 3D spatial distribution of the mPVF and tPVF are presented (Fig. 4). We compared samples B2 and B3 in order to elucidate the dependence mPVF distribution on the time of infiltration. From Fig. 4, it is seen that the amount of the monoclinic phase formation increases with respect to the infiltration time along the coating depth. However, this increase in mPVF slows down between 1 and 10 h. It is well known from the literature that the CMAS infiltration kinetics is much faster than the reaction kinetics of 7YSZ with CMAS melt [4]. This is thought to be due to the closed porosities within the coating providing an

effective barrier against CMAS infiltration into the body of the coating arms. Within the first hour the outer layers of the columns are degraded. Then the degradation of the body of the coating occurs slowly as the CMAS makes its way into the pores in the body of the coating. In time, sintering would come in to play and pore coalescence would follow. The degradation would slow down as CMAS reaches deeper in to the columns via column dissolution [16, 50].

The variation of the mPVF values shown in the box and whisker plots of sample B2 and sample B3, Fig. 4(c) and (f) respectively, lends credence to this theory. The mPVF values in sample B3 show less variation throughout the volume characterized as compared to mPVF values in sample B2. The origin of this variation between samples may be due in part to the lateral heterogeneity in mPVF values as shown in Fig. 3(g) and in Fig. 1(a). We also note the potential effect of microsampling in the variations observed between the measurements at the surface and the ones at depth $6.65\mu\text{m}$ [49]. Nonetheless the results indicate that the t-ZrO₂ phase is better preserved in sample B2, due to less time being allowed for the CMAS attack to occur. This would lead to a larger difference in values between the edges and center of the TBC columns than in sample B3.

As Raman spectroscopy reveals the chemical changes occurring in the coating, the approach can be extended to other CMAS-resistant materials. This would allow for the use of this method on one of the more promising materials used in CMAS resistant coatings. One such material, gadolinium zirconate, as well as its crystalline reaction products with CMAS, have been shown to be Raman active [51, 52]. Further, 3D confocal Raman spectroscopy has shown the ability to selectively map different phases within a material (Fig. 4). This selectivity between phases and the ability to characterize TBCs non-destructively will accelerate the development of new CMAS resistant coatings, such as those made of gadolinium zirconate. This study is anticipated to contribute to numerical models aiming to predict the lifetime of the CMAS infiltrated TBC and to advance testing techniques for in-service applications noninvasively. In future work, the effects of reaction temperature, concentration of the CMAS deposit, and annealing time will be investigated further.

The majority of the TBCs in jet engines are deposited using atmospheric plasma spraying (APS), which leads to quite heterogeneous and much thicker (300-500 μm) TBCs. It is currently unknown if this technique will work on such coatings due to extensive scattering of the incoming probe laser and outgoing signal from deep within the TBC. Here, due to the loss of signal that

occurs inside the body of the coating, the integration time of the Raman system used was 20 s to increase the signal to noise ratio. While this helped with the clarity of the spectra collected, as mentioned earlier, it caused the collection time for a single 2D map to be 8000 s leading to a time collection for 3D reconstructions that remains impractical. More work needs to be done in order to reduce the large acquisition time.

6. Conclusion

This work shows, by non-destructively probing the volume of TBCs, that the majority of thermochemical degradation resulting from the formation of the monoclinic phase occurs within the first hour of CMAS ingress. The findings indicate that at 46 μm in the coating the difference between the mPVF for B2 and B3 was only 10%, which is not high for a ten-fold annealing time. The findings also imply that the thermochemical degradation aggravates the thermomechanical degradation of coating stiffening greatly within the first hour. Further, the study provides new insights on the variability of monoclinic phase across the reacted portion of the sample due to the closed porosity and columnar microstructure of the coating. Locally, the phase transformation was observed to occur primarily closest to the inter-columnar gaps and along the column edges due to the higher exposure to the infiltrated CMAS. The observed variability of the monoclinic phase with respect to location along the depth and along the columns themselves can provide insight to the fabrication of optimized microstructures for CMAS mitigation. The significance of this work provides localized information on the degradation and infiltration in jet engine ceramic coatings, specifically highlighting the detrimental effects within the first hour of infiltration.

Acknowledgments

Funding: This material is based upon work supported by National Science Foundation grants OISE 1460045 and DMR 1337758 and by the German Aerospace Center (DLR).

Competing interests: The authors declare no conflicts of interests here.

References and Notes

- [1] M. Peters, C. Leyenes, U. Schulz, W.A. Kaysser, EB-PVD thermal barrier coatings for aeroengines and gas turbines, *Adv. Eng. Mater.* 3(4) (2001) 193-204.
- [2] X.Q. Cao, R. Vassen, D. Stoeber, Ceramic materials for thermal barrier coatings, *J. Eur. Ceram. Soc.* 24(1) (2004) 1-10.
- [3] N.P. Padture, M. Gell, E.H. Jordan, Thermal barrier coatings for gas-turbine engine applications, *Sci.* 296(5566) (2002) 280-284.
- [4] D.R. Clarke, C.G. Levi, Materials Design for the Next Generation Thermal Barrier Coatings, *Annu. Rev. Mater. Res.* 33(1) (2003) 383-417.
- [5] U. Schulz, S.G. Terry, C.G. Lev, Microstructure and texture of EB-PVD TBCs grown under different rotation modes, *Mater. sci. eng., A* 360(1) (2003) 319-329.
- [6] R. Naraparaju, M. Hüttermann, U. Schulz, P. Mechnich, Tailoring the EB-PVD columnar microstructure to mitigate the infiltration of CMAS in 7YSZ thermal barrier coatings, *J. Eur. Ceram. Soc.* 37(1) (2017) 261-270.
- [7] G. Pujol, F. Ansart, J.-P. Bonino, A. Malié, S. Hamadi, Step-by-step investigation of degradation mechanisms induced by CMAS attack on YSZ materials for TBC applications, *Surf. Coat. Technol.* 237 (2013) 71-78.
- [8] M.A. Rivera-Gil, J.J. Gomez-Chavez, C.V. Ramana, R. Naraparaju, U. Schulz, J. Muñoz-Saldaña, High temperature interaction of volcanic ashes with 7YSZ TBC's produced by APS: Infiltration behavior and phase stability, *Surf. Coat. Technol.* 378 (2019) 124915.
- [9] C. Mikulla, R. Naraparaju, U. Schulz, F.-L. Toma, M. Barbosa, L. Steinberg, C. Leyens, Investigation of CMAS Resistance of Sacrificial Suspension Sprayed Alumina Topcoats on EB-PVD 7YSZ Layers, *J. Therm. Spray Technol.* 29 (2020) 90–104.
- [10] D.L. Poerschke, C.G. Levi, Effects of cation substitution and temperature on the interaction between thermal barrier oxides and molten CMAS, *J. Eur. Ceram. Soc.* 35(2) (2015) 681-691.
- [11] R. Wellman, G. Whitman, J.R. Nicholls, CMAS corrosion of EB PVD TBCs: Identifying the minimum level to initiate damage, *Int. J. Refract. Met. Hard Mater.* 28(1) (2010) 124-132.
- [12] C.G. Levi, J.W. Hutchinson, M.-H. Vidal-Sétif, C.A. Johnson, Environmental degradation of thermal-barrier coatings by molten deposits, *MRS Bull.* 37(10) (2012) 932-941.
- [13] P. Mohan, V. Desai, Y. Sohn, T. Patterson, Degradation of Thermal Barrier Coatings by Molten CMAS (CaO-MgO-Al₂O₃-SiO₂) Deposits, 47th AIAA Aerospace Sciences Meeting including The New Horizons Forum and Aerospace Exposition, 2009.
- [14] X. Chen, Calcium–magnesium–alumina–silicate (CMAS) delamination mechanisms in EB-PVD thermal barrier coatings, *Surf. Coat. Technol.* 200(11) (2006) 3418-3427.
- [15] S. Krämer, S. Faulhaber, M. Chambers, D.R. Clarke, C.G. Levi, J.W. Hutchinson, A.G. Evans, Mechanisms of cracking and delamination within thick thermal barrier systems in aero-engines subject to calcium-magnesium-alumino-silicate (CMAS) penetration, *Mater. Sci. eng., A* 490(1) (2008) 26-35.
- [16] S. Krämer, J. Yang, C.G. Levi, C.A. Johnson, Thermochemical Interaction of Thermal Barrier Coatings with Molten CaO–MgO–Al₂O₃–SiO₂ (CMAS) Deposits, *J. Am. Ceram. Soc.* 89(10) (2006) 3167-3175.
- [17] R. Naraparaju, J.J. Gomez Chavez, P. Niemeyer, K.-U. Hess, W. Song, D.B. Dingwell, S. Lokachari, C.V. Ramana, U. Schulz, Estimation of CMAS infiltration depth in EB-PVD TBCs: A new constraint model supported with experimental approach, *J. Eur. Ceram. Soc.* 39(9) (2019) 2936-2945.

- [18] H. Peng, L. Wang, L. Guo, W. Miao, H. Guo, S. Gong, Degradation of EB-PVD thermal barrier coatings caused by CMAS deposits, *Prog. Nat. Sci.: Mat. Int.* 22(5) (2012) 461-467.
- [19] A.R. Krause, H.F. Garces, G. Dwivedi, A.L. Ortiz, S. Sampath, N.P. Padture, Calcium-magnesia-alumino-silicate (CMAS)-induced degradation and failure of air plasma sprayed yttria-stabilized zirconia thermal barrier coatings, *Acta Mater.* 105 (2016) 355-366.
- [20] O. Fabrichnaya, C. Wang, M. Zinkevich, F. Aldinger, C. Levi, Phase equilibria and thermodynamic properties of the ZrO₂-GdO₃-Y₂O₃ system, *J. Phase Equilib. Diffus.* 26(6) (2005) 591-604.
- [21] C. Mercer, S. Faulhaber, A.G. Evans, R. Darolia, A delamination mechanism for thermal barrier coatings subject to calcium-magnesium-alumino-silicate (CMAS) infiltration, *Acta Mater.* 53(4) (2005) 1029-1039.
- [22] J. Wu, H.-b. Guo, Y.-z. Gao, S.-k. Gong, Microstructure and thermo-physical properties of yttria stabilized zirconia coatings with CMAS deposits, *J. Eur. Ceram. Soc.* 31(10) (2011) 1881-1888.
- [23] R. Naraparaju, U. Schulz, P. Mechnich, P. Döbber, F. Seidel, Degradation study of 7 wt.% yttria stabilised zirconia (7YSZ) thermal barrier coatings on aero-engine combustion chamber parts due to infiltration by different CaO-MgO-Al₂O₃-SiO₂ variants, *Surf. Coat. Technol.* 260 (2014) 73-81.
- [24] A.P. Mirgorodsky, M.B. Smirnov, P.E. Quintard, Phonon spectra evolution and soft-mode instabilities of zirconia during the c-t-m transformation, *J. Phys. Chem. Solids* 60(7) (1999) 985-992.
- [25] C.M. Ramos, A.S. Tabata, P.F. Cesar, J.H. Rubo, P.A.S. Fracisconi, A.F.S. Borges, Application of micro-Raman spectroscopy to the study of yttria-stabilized tetragonal zirconia polycrystal (Y-TZP) Phase transformation, *Appl. Spectrosc.* 69(7) (2015) 810-814.
- [26] M. Ishigame, T. Sakurai, Temperature dependence of the Raman spectra of ZrO₂, *J. Am. Ceram. Soc.* 60(7-8) (1977) 367-369.
- [27] L. Hochstein, Lebensdauer von 7YSZ EB-PVD Wärmedämmschichten in Flugtriebwerken mit Lokaler CMAS Belastung: Ausfallmechanismen und Modellierung, Technische Universität Dresden, Dresden, Germany, 2017.
- [28] G. Gouadec, P. Colomban, Raman Spectroscopy of nanomaterials: How spectra relate to disorder, particle size and mechanical properties, *Prog. Cryst. Growth Charact. Mater.* 53(1) (2007) 1-56.
- [29] R. Naraparaju, U. Schulz, S. Raghavan, E. Bohorquez, Zerstörungsfreie CMAS-Infiltrationscharakterisierung von Wärmesperrbeschichtungen, (2019) DE102019107392.
- [30] R. Naraparaju, U. Schulz, S. Raghavan, E. Bohorquez, Non Destructive CMAS infiltration charecterization of Thermal barrier coatings, (2019) U.S. Patent Application No. 15/934,556.
- [31] D.R. Clarke, F. Adar, Measurement of the crystallographically transformed zone produced by fracture in ceramics containing tetragonal zirconia, *J. Am. Ceram. Soc.* 65(6) (1982) 284-288.
- [32] C.H. Perry, D.-W. Liu, R.P. Ingel, Phase Characterization of Partially Stabilized Zirconia by Raman Spectroscopy, *J. Am. Ceram. Soc.* 68(8) (1985) C-184-C-187.
- [33] P. Thompson, D.E. Cox, J.B. Hastings, Rietveld refinement of Debye-Scherrer synchrotron X-ray data from Al₂O₃, *J. Appl. Cryst.* 20(2) (1987) 79-83.
- [34] G.K. Wertheim, M.A. Butler, K.W. West, D.N.E. Buchanan, Determination of the Gaussian and Lorentzian content of experimental line shapes, *Rev. Sci. Instrum.* 45(11) (1974) 1369-1371.
- [35] R.A. Young, D.B. Wiles, Profile shape functions in Rietveld refinements, *J. Appl. Crystallogr.* 15(4) (1982) 430-438.

- [36] P. McMillan, B. Piriou, A. Navrotsky, A Raman spectroscopic study of glasses along the joins silica-calcium aluminate, silica-sodium aluminate, and silica-potassium aluminate, *Geochim. Cosmochim. Acta.* 46 (1982) 2021-2037.
- [37] S.K. Sharma, B. Simons, H.S. Yoder, Raman study of anorthite, calcium Tschermak's pyroxene, and gehlenite in crystalline and glassy states, *Am. Mineral.* 68(11-12) (1983) 1113-1125.
- [38] A.M. Hofmeister, A. Chopelas, Vibrational spectroscopy of end-member silicate garnets, *Phys. Chem. Miner.* 17(6) (1991) 503-526.
- [39] B.A. Kolesov, C.A. Geiger, Raman spectra of silicate garnets, *Phys. Chem. Miner.* 25(2) (1998) 142-151.
- [40] C.V. Raman, The vibration spectra of crystals, *Proc. Indian Acad. Sci., A* 26(339) (1947) 339-339.
- [41] E. Markevich, R. Sharabi, O. Haik, V. Borgel, G. Salitra, D. Aurbach, G. Semrau, M.A. Schmidt, N. Schall, C. Stinner, Raman spectroscopy of carbon-coated LiCoPO₄ and LiFePO₄ olivines, *J. Power Sources* 196(15) (2011) 6433-6439.
- [42] B.O. Mysen, D. Virgo, C.M. Scarfe, Relations between the anionic structure and viscosity of silicate melts—a Raman spectroscopic study, *Am. Miner.* 65(7-8) (1980) 690-710.
- [43] P. Richet, B.O. Mysen, J. Ingrin, High-temperature X-ray diffraction and Raman spectroscopy of diopside and pseudowollastonite, *Phys. Chem. Miner.* 25(6) (1998) 401-414.
- [44] B.-K. Kim, H.-o. Hamaguchi, Mode assignments of the Raman spectrum of monoclinic zirconia by isotopic exchange technique, *Phys. Status Solidi B* 203(2) (1997) 557-563.
- [45] P.E. Quintard, P. Barbéris, A.P. Mirgorodsky, T. Merle-Méjean, Comparative lattice-dynamical study of the Raman spectra of monoclinic and tetragonal phases of zirconia and hafnia, *J. Am. Ceram. Soc.* 85(7) (2002) 1745-1749.
- [46] A. Feinberg, C.H. Perry, Structural disorder and phase transitions in ZrO₂-Y₂O₃ system, *J. Phys. Chem. Solids* 42(6) (1981) 513-518.
- [47] L.A.K. Staveley, *The characterization of chemical purity: organic compounds*, Elsevier 2016.
- [48] L. Steinberg, R. Naraparaju, M. Heckert, C. Mikulla, U. Schulz, C. Leyens, Erosion behavior of EB-PVD 7YSZ coatings under corrosion/erosion regime: Effect of TBC microstructure and the CMAS chemistry, *J. Eur. Ceram. Soc.* 38(15) (2018) 5101-5112.
- [49] D.M. Lipkin, D.R. Clarke, Sample-probe interactions in spectroscopy: Sampling microscopic property gradients, *J. Appl. Phys.* 77(5) (1995) 1855-1863.
- [50] M.H. Vidal-Setif, N. Chellah, C. Rio, C. Sanchez, O. Lavigne, Calcium–magnesium–alumino-silicate (CMAS) degradation of EB-PVD thermal barrier coatings: Characterization of CMAS damage on ex-service high pressure blade TBCs, *Surf. Coat. Technol.* 208 (2012) 39-45.
- [51] Y.K. Voron'ko, A.A. Sobol, V.E. Shukshin, A.I. Zagumennyi, Y.T. Zavartsev, S.A. Kutovoi, Structural Transformations in LiGd₉(SiO₄)₆O₂ and Ca₂Gd₈(SiO₄)₆O₂ Crystals Containing Isolated [SiO₄] Complexes: Raman Spectroscopic Study, *Phys. Solid State* 54 (2012) 1635-1642.
- [52] L. Guo, M. Li, Y. Zhang, F. Ye, Improved Toughness and Thermal Expansion of Non-stoichiometry Gd_{2-x}Zr_{2+x}O₇ + x/2 Ceramics for Thermal Barrier Coating Application, *J. Mater. Sci. Technol.* 32 (2016) 28-33.

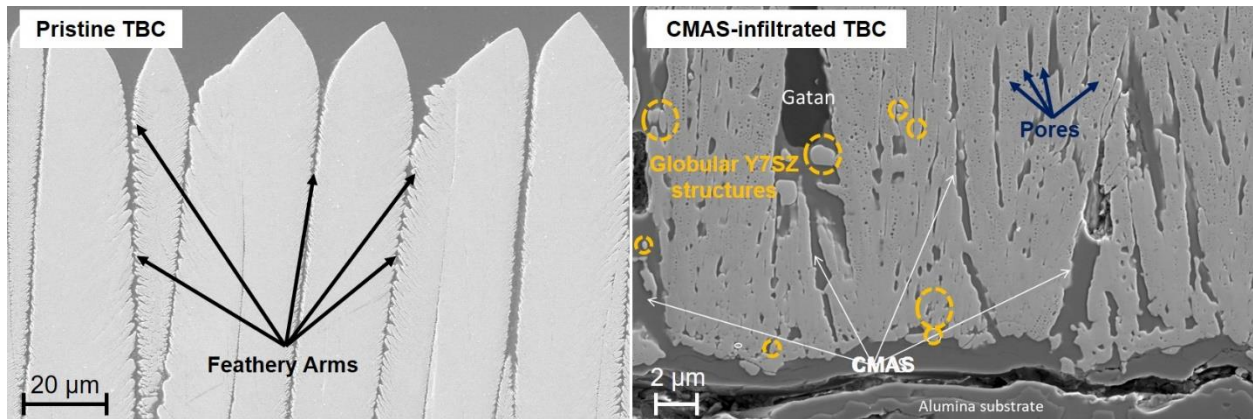


Fig. S1. (left) Feathery arms of the pristine EB-PVD TBC before infiltration by CMAS. (right) TBC after infiltration and attack by CMAS. Globular structures formed in the Y7SZ columns are indicated in yellow circles and small pores are indicated by the arrows.

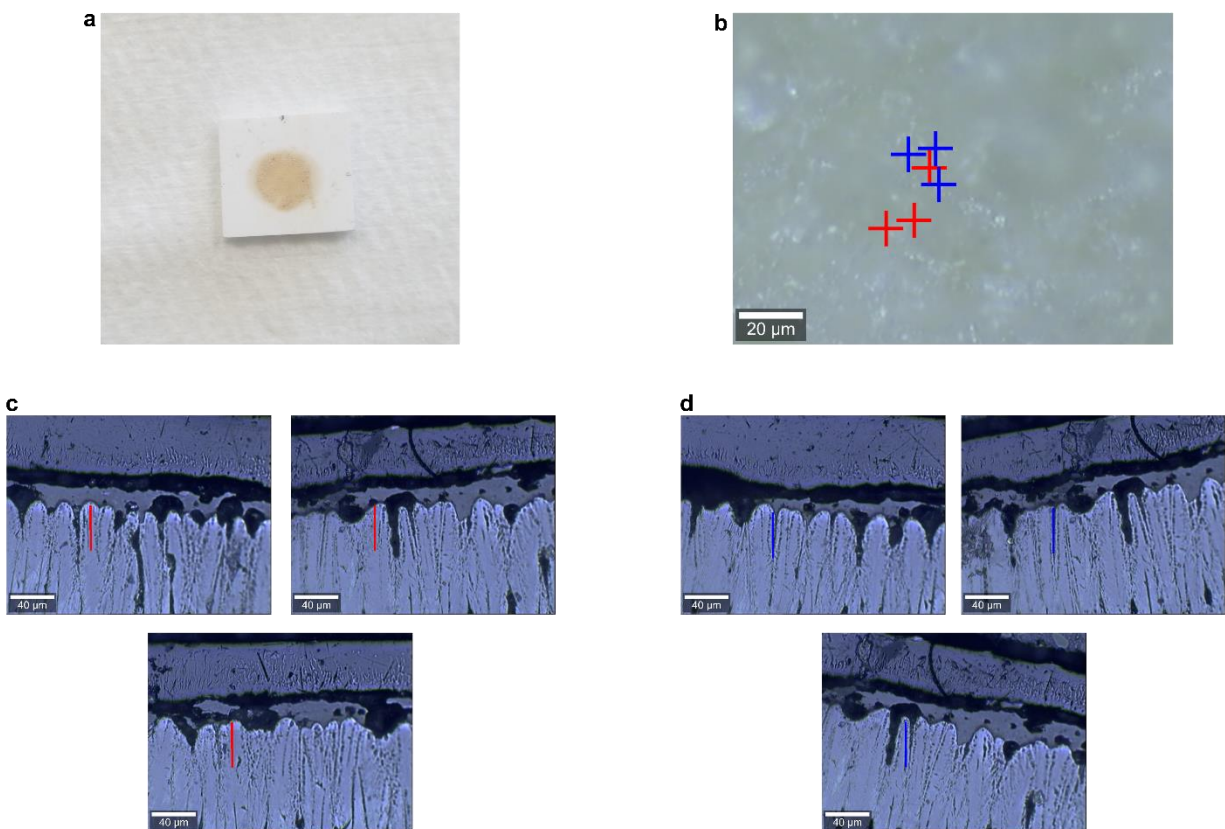


Fig. S2. (a) Optical images of the surface for confocal measurements, (b) optical image of locations where confocal measurements were taken (red for perimeter of column measurements, blue for center of column measurements) (c) optical image of location of center of column cross

sectional measurements. (d) Optical image of location of perimeter of column cross sectional measurements

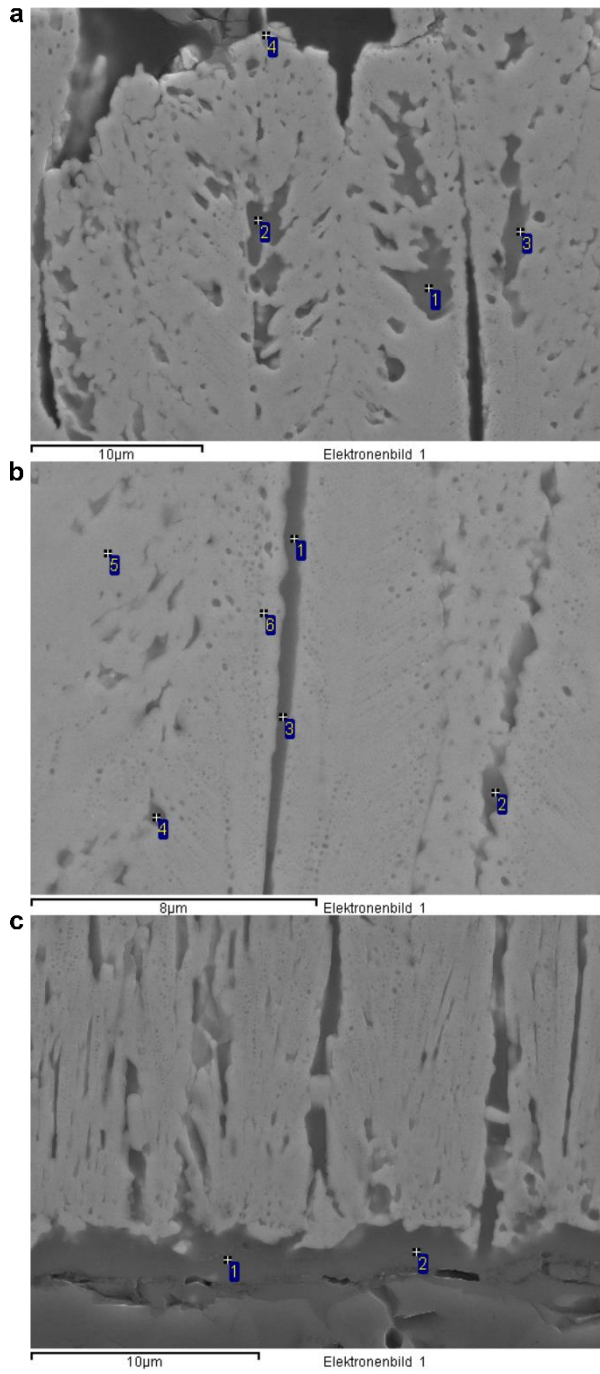


Fig. S3. SEM cross sectioned images used for SEM (a) surface, (b) middle of sample, (c) 7YSZ-alumina bond coat interface

(a)

Position	Mg	Al	Si	Ca	Ti	Fe	Zr	O
1	6.4	5.5	18.7	14.1	0.8	7.9	5.6	40.9
2	1.5	5.1	16.8	6.5	0.7	1.4	29.6	38.5
3	3.5	3.0	8.7	7.0	0.6	3.6	40.3	33.3
4	0.7	0.6	1.4	1.1	0.4	1.2	67.6	27.2

(b)

Position	Mg	Al	Si	Ca	Ti	Fe	Zr	O
1	3.5	3.6	9.3	7.9	0.5	4.2	37.2	33.8
2	2.7	3.3	8.5	7.1	0.5	3.5	41.3	33.1
3	3.1	3.2	8.3	7.2	0.5	3.8	40.8	33.0
4	2.2	2.2	5.6	5.0	0.4	3.4	50.7	30.7
5							74.0	26.0
6	0.6	0.5	1.4	1.3		1.1	68.1	27.1

(c)

Position	Mg	Al	Si	Ca	Fe	Zr	O
1	0.27	14.9	17.8	11.5	1.0	11.8	42.7
2	0.6	16.5	20.0	12.8	0.9	4.4	44.8

Fig. S4. Elemental composition (in wt%) at different locations as shown in Fig. S3 (a), (b), (c).